Nano Research

Open Access

Research Article

Breaking symmetry constraints: Structural transformation or fine-tuning of polyoxovanadate-based metal-organic polyhedra with adjustable adsorption

Meng-Yu Li[1], Ke-Wei Tong[2], Jiang-Peng Wang[1], Hong-Zhi Hu[1], Jun-Yang Wang[1], Chao-Qin Chen[2], Yang Liu[1], Lei Cai[1], Zun-Qi Liu[1] ✉, Peng Yang[2] ✉, and Yan-Hu Wang[1] ✉

[1] *College of Chemistry and Chemical Engineering, Xinjiang Agricultural University, Urumqi 830052, China*
[2] *College of Chemistry and Chemical Engineering, Hunan University, Changsha 410082, China*

Cite this article: *Nano Research*, **2025**, *18*, 94907902. https://doi.org/10.26599/NR.2025.94907902

ABSTRACT: Precise control over metal-organic polyhedra (MOPs) architectures via metal and organic linker engineering presents a critical challenge for advancing functional porous materials with specific properties. The rational design of organic linkers and secondary building units (SBUs) with programmable configurational features facilitates the assembly of novel MOPs, wherein structural complexity is enhanced through the integration of low-symmetry linkers and expandable SBUs. Herein, a series of polyoxovanadate-based metal-organic polyhedra (VMOPs) with modulated structures were systematically engineered through linker desymmetrization and SBU expansion approach. Two types of tritopic triazine (D_{3h})- or imidazole (C_s/C_1)-functionalized carboxylate ligands assemble with 3-connected prototype {V_6S} or expansional {V_6P} clusters, yielding VMOPs that exhibit structural evolution from T_d-symmetric regular tetrahedrons to D_{2d}-symmetric isosceles variants. Expansion of vertex clusters leads to structural fine-tuning of VMOPs, giving rise to diverse ligand conformations. Interestingly, these VMOPs exhibit significant differences during the iodine adsorption in both n-hexane solution and gaseous phases, which can be explained by the comprehensive influence of their cavity volume, the functional groups included, and the stacking arrangement. These findings demonstrate an effective structure-designing strategy via regulation of ligand symmetry and SBU architectural features, providing a powerful approach for the customized synthesis of MOPs with tailored structures and functionalities.

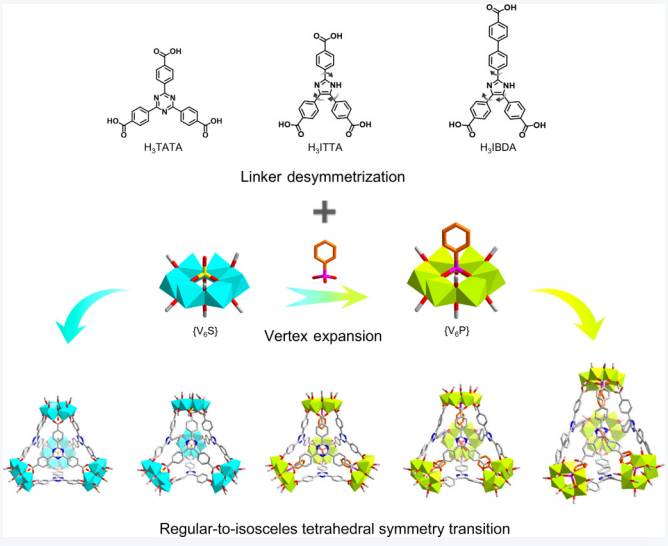

KEYWORDS: polyoxovanadates, linker desymmetrization, secondary building unit (SBU) expansion, conformation engineering, structural modulation

1 Introduction

The structural design and application exploration of functional materials have long been central pursuits for scientists [1–10]. Metal-organic polyhedra (MOPs), as hybrid materials assembled via metal ions/clusters and organic linkers through coordination bonds, are characterized by programmable architectures with confined cavities and exhibit versatile applications spanning catalysis, host–guest recognition, and environmental remediation [11–18]. Guided by reticular chemistry principles, the rational construction of functional MOP architectures for target-specific applications has flourished through synergistic modulation of metal/secondary building units (SBUs) and organic linkers [19–22].

Received: June 29, 2025; **Revised:** August 4, 2025
Accepted: August 6, 2025

✉Address correspondence to Yan-Hu Wang, 19900222wyh@163.com; Zun-Qi Liu, lzq@xjau.edu.cn; Peng Yang, pengyang216@hnu.edu.cn

As illustrated in Scheme 1, three key approaches—metal/SBU engineering, linker engineering, and linker conformation engineering—are typically employed to enable structural diversification and functional realization of MOPs. While these synthetic approaches have been rigorously established in metal-organic frameworks (MOFs) for architectural customization and performance optimization [23–31], their implementation in MOPs remains conspicuously underdeveloped. To the best of our knowledge, MOP synthetic methodologies demonstrate inherent differences when compared to MOF systems. For instance, during metal/SBU engineering, various clusters frequently exhibit concave structural features, with terminal capping groups at one end to preclude their extension into network architectures, which fundamentally distinguishes them from metal nodes in MOF structures. Furthermore, their connectivity is less extensively interconnected than that in MOFs; instead, they exhibit lower connection numbers, as exemplified by 2-connected Mo-SBU [32], 3-connected Zr-SBU [33], 4-connected Co-SBU [34], and 5-

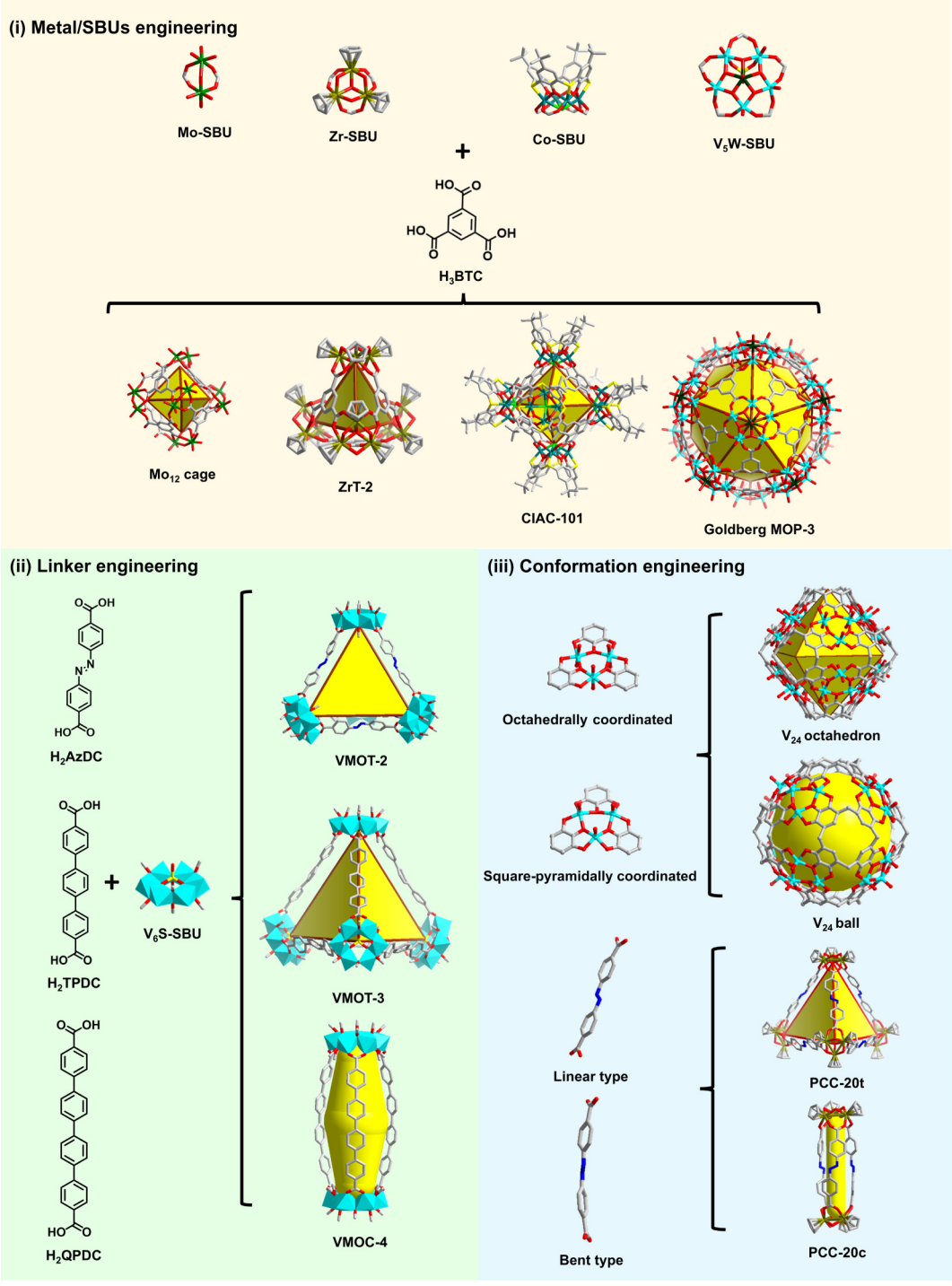

Scheme 1 Schematic representation of the three strategies for customized synthesis of MOPs: (i) Metal/SBUs engineering, (ii) linker engineering, and (iii) conformation engineering.

connected V_5W-SBU [35]. To date, no examples beyond 5-connected have been documented, with this deliberate constraint ensuring the assembly of discrete molecular entities. Consequently, when coordinating with identical linkers, these entities adopt distinct geometric configurations such as tetrahedral, octahedral, and Goldberg architectures (Scheme 1(i)).

Complementary to metal/SBU engineering, linker engineering and conformation engineering, which rely on ligand characteristics, have become effective strategies to expand the structural diversity of MOPs. Linker engineering is established by precisely regulating ligand configurations, symmetry, and functional motifs, while conformation engineering refers to the diverse conformations exhibited by the same ligand in materials with different topologies assembled under distinct reaction conditions. Linker engineering has proven instrumental in the assembly of MOFs, as exemplified by classical systems such as UiO-66, UiO-67, and UiO-68 [36]. These MOFs maintain the same topological type upon ligand elongation while achieving cavity expansion. In contrast, the MOPs domain reveals a markedly different scenario: ligand extension drives a structural evolution in 3-connected V_6S-SBU-based architectures, progressing from regular tetrahedra to metastable tetrahedral intermediates and ultimately capsule-like configurations [37] (Scheme 1(ii)). Furthermore, linker functionalization [38] or installation [39] not only broadens the application scope of MOPs but also modulates their packing modes, such as interlocked dimers or dense packing arrangements [40, 41]. By precisely modifying reaction conditions or introducing modulators, conformational diversity of linkers in MOPs can be induced, enabling localized structural adjustments or complete topological transformations of assemblies—embodying the essence of conformation engineering. However, conformational engineering remains uncommon in the structural assembly of MOPs due to the inherent rigidity of metal clusters. For example, solvent modulation enables precise control over the coordination mode of V_3-SBUs, facilitating reversible switching between octahedral and spheroidal architectures in the assembled structures, while the linkers exhibit dynamic contraction/expansion conformational features [42]. Significantly, linear semi-flexible azo-bridged ligands induce dynamic disorder in tetrahedral coordination cages, which can be driven to ordered bent states via conformational modulation in capsules with a narrow cavity (Scheme 1(iii)) [43].

Conformation engineering has empowered MOFs to exhibit remarkable architectural variety. Ligand desymmetrization approaches further enhance this structural diversity by amplifying ligand flexibility [29, 30, 44, 45]. However, the assembly of MOPs predominantly relies on rigid vertex clusters, necessitating ligands with high symmetry for structural construction. This inherent structural requirement has left ligand desymmetrization approaches largely unexplored in MOP synthesis. If the symmetry of the ligands is altered, the structure of the assembled MOPs will also undergo corresponding modifications. In metal-oxo cluster chemistry [46–55], the diverse coordination modalities of vanadium-oxo clusters endow them as superior vertex candidates for the assembly of MOPs. Zaworotko, Su, Wang and Fang have developed a new class of MOPs based on 3-connected $[V^{IV}_6O_6(OCH_3)_9(SO_4)(COO)_3]^{2-}$ ({V_6S}) [56], $[V^{IV}_6O_6(OCH_3)_9(V^{V}O_3)(H_2O)(COO)_3]^{-}$ ({V_7}) [57], $[V^{IV}_6O_6(OCH_3)_9(PhPO_3)(COO)_3]^{2-}$ ({V_6P}) [58, 59], 4-connected $[V^{V}_4O_8Cl(COO)_4]^{-}$ ({V_4Cl}), $[V^{IV}_4V^{V}O_9Cl(COO)_4]^{2-}$ ({V_5Cl}) [60, 61], and 5-connected $[V^{IV}_5O_{10}(SO_4)(COO)_5]^{7-}$ ({V_5S}) [62], $[W^{VI}V^{IV}_5O_{11}(SO_4)(COO)_5]^{3-}$ ({V_5W}) [35] as vertices, providing cage-like materials that exhibit both novel architectures and functional properties (Section S2 in the Electronic Supplementary Material (ESM)). Among these numerous structures, scientists have focused more on the construction and functionalization of regular polyhedra assembled from highly symmetrical ligands, while exploration of irregular polyhedra has received comparatively less attention [37, 40, 41, 63–69]. Against this backdrop, we strategically selected three tritopic carboxylate ligands with distinct symmetry profiles: D_{3h}-symmetric 4,4',4''-(1,3,5-triazine-2,4,6-triyl)tribenzoic acid (H_3TATA), along with C_s or C_1-symmetric 4,4',4''-(1H-imidazole-2,4,5-triyl)tribenzoic acid (H_3ITTA) and 4,4'-(2-(4'-carboxy-[1,1'-biphenyl]-4-yl)-1H-imidazole-4,5-diyl)dibenzoic acid (H_3IBDA). Through systematic assembly of these ligands with prototype {V_6S} or expansional {V_6P} clusters, we constructed polyoxovanadate-based metal-organic tetrahedra (VMOTs) that exhibit a controlled structural evolution from T_d-symmetric regular architectures (**R-VMOT-1**, **R-VMOT-P-1**; R = regular) to D_{2d}-symmetric isosceles variants (**I-VMOT-1**, **I-VMOT-P-1**, **I-VMOT-P-2**; I = isosceles). In examining the structures of **R-VMOT-1** and **R-VMOT-P-1**, it is evident that despite maintaining their fundamental structural type, alterations in vertex configurations play a pivotal role in facilitating localized modifications to both structural dimensions and cavity characteristics. Remarkably, analogous structural modulations were also observed within isohedral tetrahedra (**I-VMOT-1** and **I-VMOT-P-1**). The conformational features of each ligand in these tetrahedra were meticulously analyzed. Finally, **TMA-R-VMOT-P-1**, **TMA-I-VMOT-P-1**, and **TMA-I-VMOT-P-2** were selected as adsorption candidates owing to their unique cavities, functional group distributions, and packing patterns, enabling targeted iodine capture in both n-hexane and gaseous phases. Interestingly, **TMA-I-VMOT-P-2** exhibits faster adsorption kinetics toward iodine in n-hexane, whereas **TMA-I-VMOT-P-1** demonstrates superior adsorption capacity for gaseous iodine. More broadly, these findings demonstrate that linker desymmetrization and SBU expansion enable structural modulation of MOPs, thereby regulating their adsorption performance.

2 Results and discussion

2.1 From regular to isosceles tetrahedra: ligand desymmetrization-driven transition

The symmetry of ligands critically governs the structural topologies of MOPs. H_3TATA (Fig. 1(a)), exhibiting D_{3h} point group symmetry in free state, self-assembles with {V_6S} (Fig. 1(b)) to form a perfect tetrahedral **R-VMOT-1** with T_d symmetry (Fig. 1(d)) [70]. Drawing inspiration from this triazine group, we endeavored to design imidazole-based H_3ITTA and H_3IBDA (Fig. 1(a)). In novel MOF architectures [29], H_3ITTA exhibits lower C_s or C_1 symmetry, while the similar yet unexplored H_3IBDA may also display C_s or C_1 symmetry under specific conditions. H_3ITTA and H_3IBDA were synthesized according to a previously reported method [71–73] and confirmed by ^1H NMR (Section S3 in the ESM). We subsequently carried out the assembly of these low-symmetry ligands with {V_6S} clusters to investigate how conformational changes in the ligands affect the structures of the assembled tetrahedra (Section S4 in the ESM). When H_3ITTA was treated with $VOSO_4$ in the mixed solvent of N,N-dimethylformamide (DMF)/CH_3OH at 150 °C for 60 h, yellow-green diamond-shaped crystals of **I-VMOT-1** were

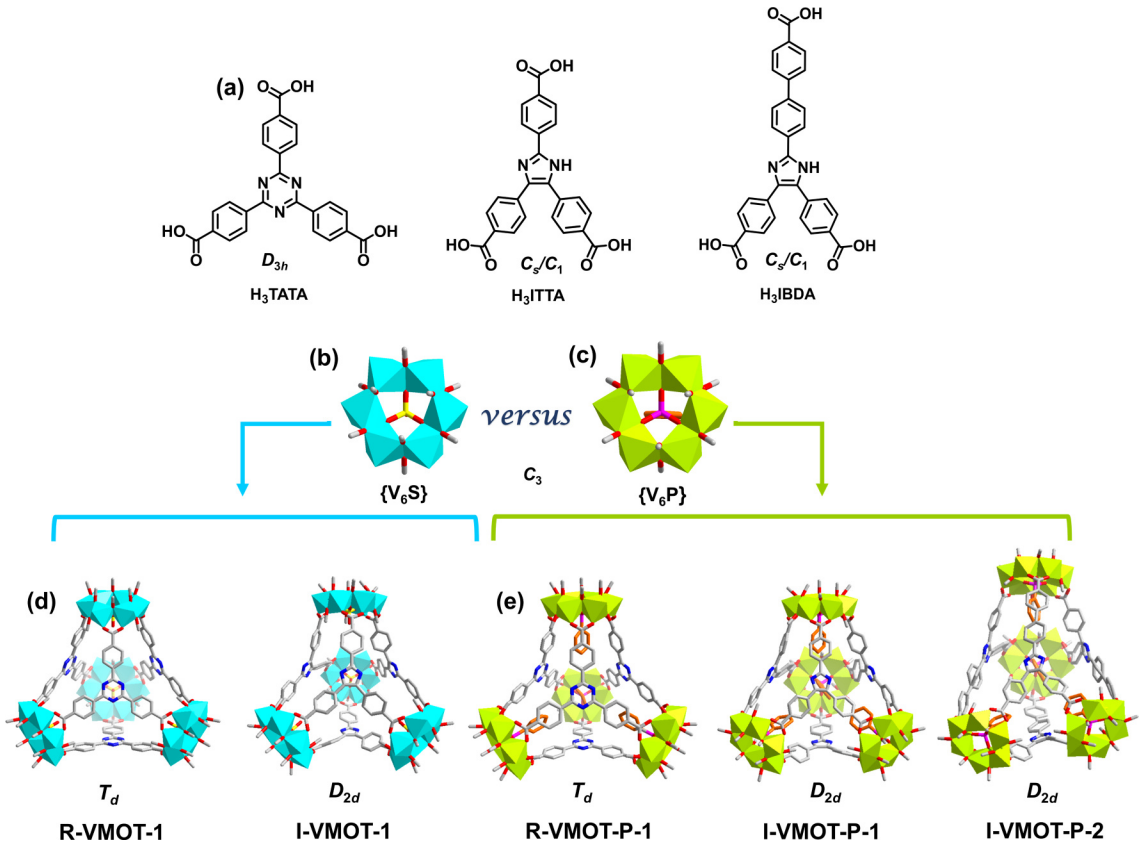

Figure 1 (a) Tritopic carboxylate ligands with different point group symmetry characteristics used in the synthesis. (b) and (c) Polyhedra-and-stick representation of {V_6S}, {V_6P} with C_3 symmetry. (d) Polyhedra-and-stick representations of **R-VMOT-1** and **I-VMOT-1**, constructed from {V_6S} units, display T_d and D_{2d} symmetries, respectively. (e) The molecular structures of **R-VMOT-P-1** (T_d), **I-VMOT-P-1** (D_{2d}) and **I-VMOT-P-2** (D_{2d}), based on {V_6P} clusters and demonstrating structural evolutionary traits. These structures were elucidated through X-ray crystallography. Color code: {VO_6}, turquoise or chartreuse octahedra; P, pink; S, yellow; O, red; N, blue; C, grey or orange. Hydrogen atoms are omitted for clarity.

obtained successfully (Fig. 1(d)). Single-crystal X-ray diffraction reveals that **I-VMOT-1** crystallizes in the monoclinic space group *C*2/*c* (Section S5 in the ESM), comprising four {V_6S} clusters bridged by four $ITTA^{3-}$ linkers to form a discrete V_4F_4-type tetrahedral coordination cage (where V = vertex, F = face). It has an anionic composition of $\{[V_6O_6(OCH_3)_9(SO_4)]_4(ITTA)_4\}^{8-}$, with four molecules in the unit cell (V = 34,079 Å^3, Table S1 in the ESM). The asymmetric unit of **I-VMOT-1** is composed of two {V_6S} clusters, two $ITTA^{3-}$ ligands, three DMF molecules, and four tetramethylammonium (TMA^+) counter ions (Fig. S11 of Section S6 in the ESM). The TMA^+ ions are thought to derive from the thermal decomposition of DMF solvent molecules in the presence of CH_3OH [74], which serves to neutralize the negative charge of the anionic moieties. The formula of its TMA salts is $(TMA)_8\{[V_6O_6(OCH_3)_9(SO_4)]_4(ITTA)_4\}\cdot17CH_3OH\cdot20DMF$. In comparison to **R-VMOT-1**, the imidazole-functionalized **I-VMOT-1** possesses a distorted molecular geometry. The overall architecture of **I-VMOT-1** manifests as an isosceles tetrahedron (D_{2d}), with ligand-vertex connectivity patterns explicitly resolved in the crystallographic model (Fig. 1(d)). All six vanadium ions constituting the {V_6S} vertex adopt the +4 oxidation state, consistent with prior observations [56], and validated by bond valence sum (BVS) calculations (Table S2 in the ESM). X-ray photoelectron spectroscopy (XPS) measurements were performed on **I-VMOT-1**, where the binding energy of the V $2p_{3/2}$ peak is 516.0 eV, further validating the above findings (Fig. S12 in the ESM). The phase purity of the bulk products was verified by comparing the experimental powder X-ray diffraction (PXRD) diffractograms with the simulated patterns (Fig. S13 in the ESM). Infrared spectroscopy and thermal stability analysis data provide additional insights into the physicochemical properties of the distorted tetrahedral cage (Figs. S14 and S15 in the ESM). To verify this conclusion and fabricate a tetrahedral cage with enhanced distortion, we opted for the bulkier ligand H_3IBDA to assemble with {V_6S}. Despite comprehensive experimental trials under diverse conditions, crystalline materials were not successfully obtained. This implies that the extended ligand poses challenges for its assembly with {V_6S}, potentially due to the instability of the resulting cage.

In a separate case, upon replacing the vertex cluster with expansional {V_6P} (Fig. 1(c)), three ligands of distinct configurations are each able to form the corresponding cages:

$(TMA)_8\{[V_6O_6(OCH_3)_9(PhPO_3)]_4(TATA)_4\}\cdot31CH_3OH\cdot8DMF$ (**TMA-R-VMOT-P-1**)

$(TMA)_8\{[V_6O_6(OCH_3)_9(PhPO_3)]_4(ITTA)_4\}\cdot15CH_3OH\cdot8DMF$ (**TMA-I-VMOT-P-1**)

$(TMA)_8\{[V_6O_6(OCH_3)_9(PhPO_3)]_4(IBDA)_4\}\cdot19CH_3OH\cdot17.5DMF$ (**TMA-I-VMOT-P-2**)

As anticipated, the assembled **R-VMOT-P-1** from H_3TATA and {V_6P} exhibits minor adjustments in specific details (Table S3 in the ESM); however, it still retains a regular tetrahedral configuration (Fig. 1(e)). Based on the experience of our research group, the incorporation of phenylphosphonic acid can effectively functionalize the interior of the tetrahedral cavity and facilitate the

crystallization of VMOPs. During the assembly process, the weak interactions between phenylphosphonic acid and the peripheral ligands play a significant role in the formation and stabilization of the structure [37, 40, 41, 63]. When H_3ITTA or the bulkier H_3IBDA ligand is assembled with {V_6P}, the resulting isosceles **I-VMOT-P-1** and **I-VMOT-P-2** (Fig. 1(e)) exhibit enhanced distortion proportional to ligand size. Owing to their low symmetry, the discrete cages of **I-VMOT-P-1** and **I-VMOT-P-2** crystallize in the monoclinic system through mutual packing, where **I-VMOT-P-1** belongs to the *C*2/*c* space group and **I-VMOT-P-2** to the *P*2/*c* space group. The minimum asymmetric unit in compound **I-VMOT-P-1** is represented by half of an intact isosceles tetrahedral cage, while in compound **I-VMOT-P-2**, it is characterized as a complete isosceles tetrahedral cage generated through the adjacent stacking of two half-cages (Fig. S11 in the ESM). The extent of distortion in tetrahedral architecture governs its crystallization behavior, a feature that encapsulates the fascination of crystalline materials. Finally, and importantly, it is essential to note that the actual point-group symmetry of a molecule in crystals is constrained by its positional symmetry. Taking **I-VMOT-1** as an example, its overall molecular geometry approximates an isosceles tetrahedron with D_{2d} point group symmetry, despite its crystallographic site symmetry being lower. Consequently, the structural types of the synthesized VMOPs can be efficiently modulated by varying the symmetry of the ligands.

2.2 Structural fine-tuning of tetrahedra via vertex expansion

To better compare the geometric differences among these VMOTs caused by vertex expansion, we meticulously analyzed the dihedral angle between two phenyl rings in the organic ligands. For clarity, the phenyl rings are labeled P1, P2, and P3, respectively. The dihedral angles between adjacent phenyl rings (P1-P2, P2-P3, P3-P1) are presented in Fig. 2(a) and Fig. S16 in the ESM. Both {V_6S} and {V_6P} exhibit characteristics that are closely aligned with C_3 symmetry. By substituting the sulfate group at the center of {V_6S} with phenylphosphonic acid, a structural transformation from {V_6S} to {V_6P} can be realized (Fig. S17 in the ESM). Such modifications lead to the expansion of vertex clusters, enabling more precise adjustments within the assembly structure (Table S3 in the ESM). For visual clarity, dihedral angles are presented as coordinate plots (Fig. S18(a) in the ESM). The dihedral angles are measured as 0.69°, 0.68°, and 0.68° for **R-VMOT-1** and 6.56°, 6.56°, and 6.54° for **R-VMOT-P-1**, respectively (Fig. 2(a)). The angles α, β, and γ in **R-VMOT-1** are all equal to 60.00°, thereby forming equilateral triangular faces (Fig. 2(b) and Table S4 in the ESM). From this observation, it can be concluded that the tetrahedron formed by connecting μ_3-S in **R-VMOT-1** has equal edge lengths of 15.99 Å, thereby further confirming that this tetrahedron is regular (Fig. 2(b)). For **R-VMOT-P-1**, the angles α, β, and γ are identical to those in **R-VMOT-1**; however, the edge lengths are adjusted to

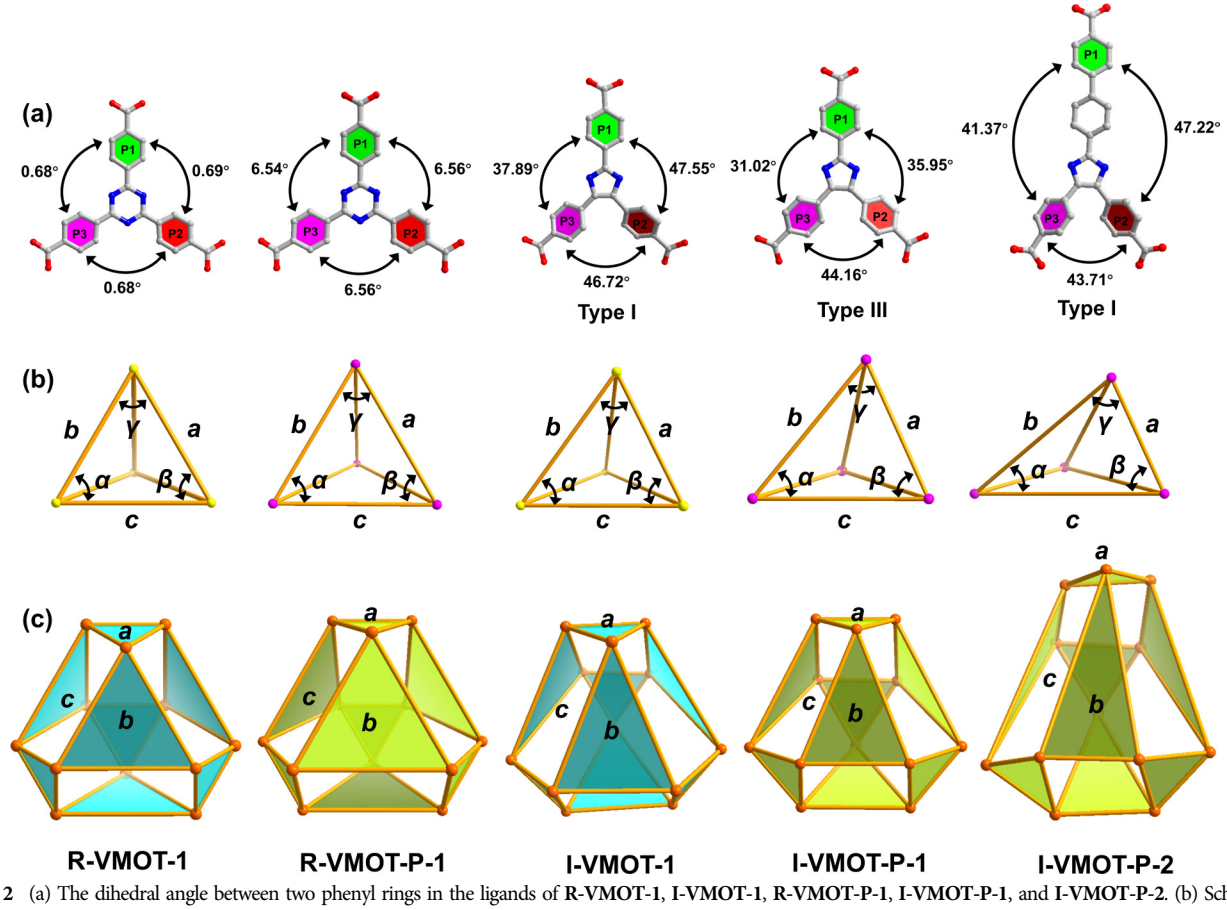

Figure 2 (a) The dihedral angle between two phenyl rings in the ligands of **R-VMOT-1**, **I-VMOT-1**, **R-VMOT-P-1**, **I-VMOT-P-1**, and **I-VMOT-P-2**. (b) Schematic representations of regular- and isosceles tetrahedra are created by connecting four S or P atoms in the VMOTs, illustrating the lengths and angles of the simplified tetrahedra. (c) Polyhedral models of this series, in which the carbon atoms in carboxylate groups of the organic ligands are purposefully selected as vertices of VMOTs, carboxylate-based MBBs ($[V_6O_6(OCH_3)_9(SO_4)(CO_2)_3]^{2-}$ or $[V_6O_6(OCH_3)_9(PhPO_3)(CO_2)_3]^{2-}$) and organic linkers can be acted as faces. Color code: P, pink; S, yellow; O, red; N, blue; C, grey. Hydrogen atoms are omitted for clarity.

16.22 Å due to the incorporation of phenylphosphonic acid, which induces an expansion of the vertex cluster. From another perspective, by connecting the carbon atoms at the two farthest vertices of the tetrahedron, it can be observed that the distance in **R-VMOT-P-1** is longer than that in **R-VMOT-1**, further confirming that vertex expansion induces subtle adjustments in the tetrahedral architecture (Fig. S19 in the ESM). In contrast to the regular structures derived from H_3TATA, those constructed from H_3ITTA exhibit a significant degree of distortion. Regardless of {V_6S} or {V_6P}, assembly with H_3ITTA yields an isosceles tetrahedron where each prism and its opposing counterpart are consistently equivalent. In **I-VMOT-1** and **I-VMOT-P-1**, the phenyl rings in the ligands are tilted relative to each other, giving dihedral angles of 47.55°, 46.72°, and 37.89° for **I-VMOT-1** and 35.95°, 44.16°, and 31.02° for **I-VMOT-P-1**, respectively (Fig. 2(a) and Fig. S18(a) in the ESM). The non-coplanarity of the ligands is a key factor contributing to the irregularities observed in the tetrahedra. The isosceles triangular faces of the distorted structures in **I-VMOT-1** and **I-VMOT-P-1** exhibit angle values of α = 51.17°, β = 64.84°, γ = 63.98° for **I-VMOT-1** and α = 50.49°, β = 64.98°, γ = 64.53° for **I-VMOT-P-1**, respectively. The corresponding side lengths *a*, *b*, *c* for angles α, β, γ are 13.97, 16.12, and 16.23 Å for **I-VMOT-1** and 13.97, 16.41, and 16.35 Å for **I-VMOT-P-1**, respectively (Fig. 2(b) and Table S4 in the ESM). The line connecting the carbon atoms at the two farthest vertices of the tetrahedron also reveals subtle structural expansion caused by vertex cluster expansion (Fig. S19 in the ESM). It is evident that two of the edge lengths are closely matched in value, while the third edge length shows a substantial difference. When one arm of H_3ITTA is further elongated to form H_3IBDA, the resulting isosceles tetrahedron exhibits more pronounced distortion. In the structure of **I-VMOT-P-2**, the dihedral angles of the ligand are measured as 47.22°, 43.71°, and 41.37° (Fig. 2(a) and Fig. S18(a) in the ESM). The angles α, β, and γ are 36.02°, 69.54°, and 74.43°, respectively, with corresponding side lengths *a*, *b*, and *c* of 12.50, 19.91, and 20.47 Å (Fig. 2(b) and Table S4 in the ESM).

Polyhedral models of this series offer a more intuitive depiction of the structural regulation (Fig. 2(c)). These polyhedra exhibit analogous yet progressively distorted geometries when the polyoxovanadate-based building blocks and organic ligands are considered as triangular faces (Fig. 2(c), *a* or *b*). Additionally, the presence of a rectangular window (Fig. 2(c), *c*) is evident. The triangular and rectangular windows of **R-VMOT-1** exhibit dimensions of 6.84 Å × 6.84 Å × 6.84 Å, 12.14 Å × 12.14 Å × 12.14 Å, and 6.84 Å × 12.14 Å × 6.84 Å × 12.14 Å, respectively (Fig. 2(c) and Table S5 in the ESM). For **R-VMOT-P-1**, the dimensions of these triangular and rectangular windows change to 6.92 Å × 6.92 Å × 6.92 Å, 12.17 Å × 12.17 Å × 12.17 Å, and 6.92 Å × 12.17 Å × 6.92 Å × 12.17 Å, respectively (Fig. 2(c) and Table S5 in the ESM). These data further confirm the role of vertex expansion in the local regulation of the assembled tetrahedra. For isosceles tetrahedra, the situation is somewhat more complex. In their triangular or rectangular faces, the edge lengths are not entirely equal, which is attributed to the reduced symmetry of the ligands. The dimensions of the triangular and rectangular windows in **I-VMOT-1** are 6.89 Å × 6.92 Å × 6.97 Å, 9.79 Å × 12.69 Å × 12.80 Å, and 6.96 Å × 12.69 Å × 6.97 Å × 12.71 Å, respectively (Fig. 2(c) and Table S5 in the ESM). Similarly, expansion is observed in tetrahedra with {V_6P} as vertices, and the corresponding values for triangular and rectangular faces are 6.92 Å × 6.94 Å × 7.00 Å, 9.63 Å × 12.77 Å × 12.87 Å, and 6.94 Å × 12.80 Å × 7.11 Å × 12.87 Å, respectively (Fig. 2(c) amd Table S5 in the ESM). For **I-VMOT-P-2**, the numerical values of triangular and rectangular faces reveal more severe distortion, with dimensions of 6.95 Å × 7.06 Å × 7.07 Å, 8.27 Å × 16.99 Å × 17.29 Å, and 6.92 Å × 17.29 Å × 6.95 Å × 17.32 Å, respectively (Fig. 2(c) and Table S5 in the ESM). The structural analysis presented above demonstrates that the shape of the vertices can effectively regulate the geometry of tetrahedral coordination cages.

2.3 Linker conformation analysis in different MOPs

To further investigate the distinctions among such structures, the conformations and symmetries of the ligands have drawn our attention. For clarity, the central imidazole or triazine functional moiety is denoted as F, while the peripheral phenyl rings are sequentially labeled P1, P2, and P3 (Fig. 3). The dihedral angles between adjacent rings (P1-F, P2-F, P3-F) and between each peripheral phenyl ring and its corresponding carboxylate moiety (P1-COO, P2-COO, P3-COO) are presented in Fig. S18(b) in the ESM. Dihedral angle analysis indicates that all angles fall within the range of 0.39°–50.73°, and this non-coplanar nature gives rise to diverse conformations. Due to the high symmetry of H_3TATA, it exhibits D_{3h} symmetry. In **R-VMOT-1**, H_3TATA retains this high symmetry, and the tetrahedron assembled with {V_6S} exhibits perfect T_d point group symmetry characteristics (Fig. 3(a), Type I, Fig. S18(b) in the ESM). However, in **R-VMOT-P-1**, the expansion of {V_6P} causes the triazine group of H_3TATA and the three phenyl rings at the 1, 3, 5-positions to no longer lie in the same plane, resulting in a Type II conformation with symmetry reduced to C_{3v}. The local minor structural modification arises from SBU engineering, where H_3TATA is compelled to adopt different conformations to form a closed cage with distinct vertex clusters (Fig. 3(a), Type II, Fig. S18(b) in the ESM). The decreased symmetry of H_3ITTA enhances its rotational flexibility, causing the two ligands within the minimal asymmetric unit of **I-VMOT-1** to exhibit different conformations: Type I and Type II (Fig. 3(b) and Fig. S18(b) in the ESM). In contrast to the symmetry lowering in **R-VMOT-P-1** caused by bending of edge ligands, Type I and Type II in **I-VMOT-P-1** adopt low-symmetry C_1 conformations through rotation, which is distinct from the C_s symmetry observed in the MOF architecture [27]. In Type I and Type II, the direction of phenyl ring rotation is the same, with the difference lying in the rotation angles. In Type III and Type IV, the diverse rotation directions of phenyl rings further confirm the subtle structural modulation caused by vertex expansion (Fig. 3(c) and Fig. S18(b) in the ESM). Despite distinct conformational pathways, H_3ITTA displays C_1-symmetry across all conformations. In **I-VMOT-P-2**, the phenyl rings in Type I and Type II rotate in exactly opposite directions while still exhibiting C_1-symmetry (Fig. 3(d) and Fig. S18(b) in the ESM). Additionally, the diverse dihedral angles between the plane of the carboxyl group and its corresponding phenyl ring arise from the mutual fitting required for the ligand and vertex to co-assemble into a closed structure (Fig. S18(b) in the ESM).

2.4 Adjustable iodine adsorption features

Nuclear energy has long been recognized as a clean and reliable energy source, garnering considerable attention worldwide. However, radioactive iodine, a byproduct of nuclear industry waste, exists as a highly mobile gaseous species with significant water solubility, thereby posing a substantial risk to both ecological systems and human health [75, 76]. Abundant research has shown

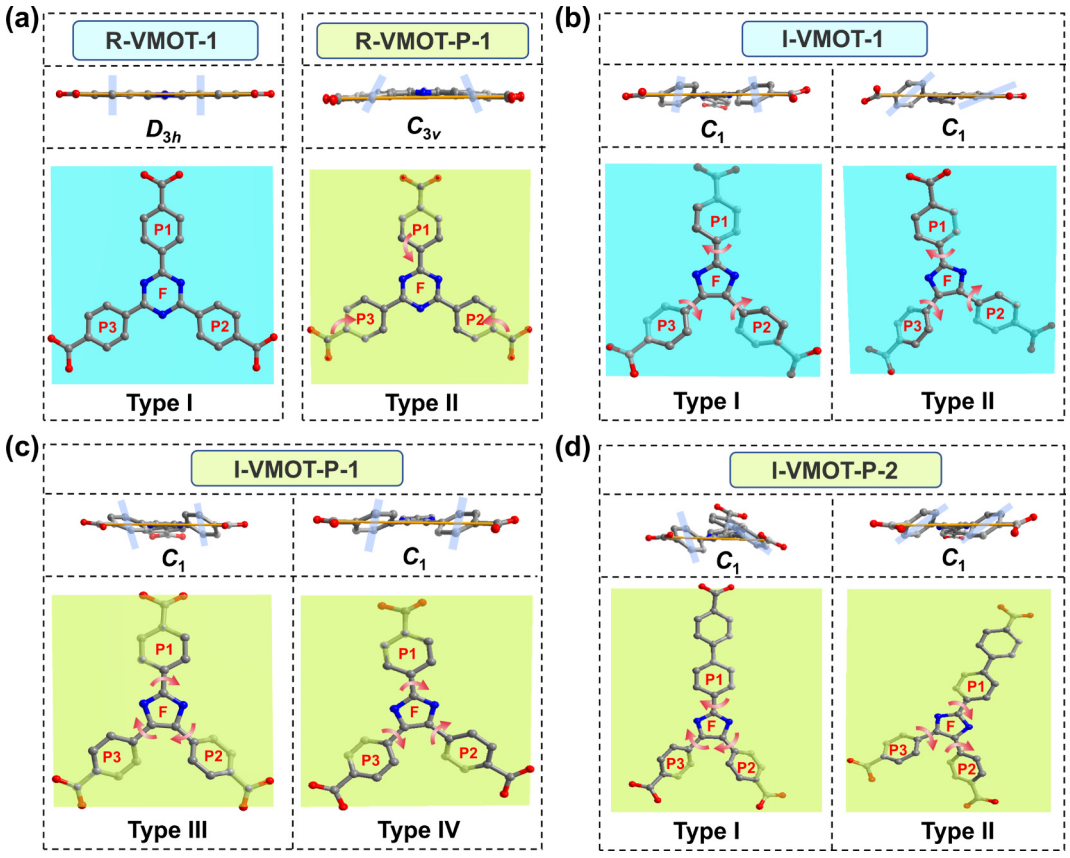

Figure 3 (a) The conformational features of H_3TATA in **R-VMOT-1** and **R-VMOT-P-1**, respectively. (b) and (c) The low-symmetry H_3ITTA in **I-VMOT-1** and **I-VMOT-P-1** exhibits diverse conformational features. (d) The conformational behavior of H_3IBDA in **I-VMOT-P-2**, induced by flexible single-bond rotation. Color code: O, red; N, blue; C, dark grey. Hydrogen atoms are omitted for clarity.

that aromatic rings and nitrogen-containing groups exhibit a strong tendency to interact with iodine via specific host–guest interactions [75–79]. The study of adsorption behavior in cage-like materials necessitates thorough evaluation of their structural cavity volumes, embedded functional groups, and spatial packing arrangements, as these significantly influence their functional properties. **TMA-R-VMOT-P-1**, **TMA-I-VMOT-P-1**, and **TMA-I-VMOT-P-2** were employed as adsorbents, as the substitution of sulfate groups with benzenephosphonic acid in their structures alters hydrophilicity, providing an advantage for iodine adsorption [80]. The cavity volumes of these materials, calculated using the MoloVol program [81], are 487.68 Å^3 for **R-VMOT-P-1**, 487.50 Å^3 for **I-VMOT-P-1**, and 743.05 Å^3 for **I-VMOT-P-2**, respectively. The triazine and imidazole moieties in the three MOPs are both nitrogen-containing groups. Although the number of nitrogen atoms varies, they all facilitate iodine adsorption. The packing of these discrete cages through supramolecular weak interactions is depicted in Fig. 4. In the structural packing of **R-VMOT-P-1**, each tetrahedron is surrounded by eight neighboring tetrahedra via strong C–H···π interactions, forming a three-dimensional open supramolecular framework with classic ***bcu*** topological features (Figs. 4(a) and 4(b), Fig. S20 in the ESM). Two distinct types of channels are observed along the crystallographic axes (Fig. 4(c)). Channel A, measuring 10.02 Å × 10.02 Å, is situated within the window of the tetrahedron, while channel B, which arises from the packing of four adjacent tetrahedron, has dimensions of approximately 12.15 Å × 12.15 Å (Fig. 4(c)). The potential solvent-accessible volumes for **TMA-R-VMOT-P-1**, as calculated using the PLATON program [82], were determined to be 11,059.5 Å^3, accounting for 55.7% of the total crystal volume. These substantial voids are predominantly occupied by TMA^+ and solvent molecules. In the structures of **I-VMOT-P-1**, and **I-VMOT-P-2**, each isosceles tetrahedron is linked to four adjacent tetrahedra through strong C–H···π or π···π interactions, leading to the formation of two-dimensional layered polymers (Figs. 4(d), 4(e), 4(g) and 4(h)). Similarly, two types of channels with distinct sizes are observed in the packing structure of **I-VMOT-P-1**, measuring 5.37 Å × 5.56 Å and 4.22 Å × 14.73 Å for channel A and B, respectively (Fig. 4(f)). For **I-VMOT-P-2**, the channel A formed by tetrahedral packing measure 10.68 Å × 5.92 Å (Fig. 4(i)). The PLATON program analysis revealed that the two-dimensional supramolecular polymers exhibit potential solvent-accessible areas of 16,560.3 and 16,299.8 Å^3 for **I-VMOT-P-1** and **I-VMOT-P-2**, respectively, corresponding to 47.9% and 46.0% of their total crystal volumes.

In this context, the iodine adsorption performance of **TMA-R-VMOT-P-1**, **TMA-I-VMOT-P-1**, and **TMA-I-VMOT-P-2** was systematically evaluated in n-hexane solution and as iodine vapor (Fig. S21 of Section S7 in the ESM). As shown in Figs. 5(a)–5(c), both three compounds could capture iodine in n-hexane solution. It is evident that **TMA-I-VMOT-P-2** demonstrates significantly enhanced loading capacity and adsorption rate compared to **TMA-R-VMOT-P-1** and **TMA-I-VMOT-P-1**. The equilibrium adsorption capacities of **TMA-R-VMOT-P-1**, **TMA-I-VMOT-P-1**, and **TMA-I-VMOT-P-2** were determined to be 46.21, 45.58, and

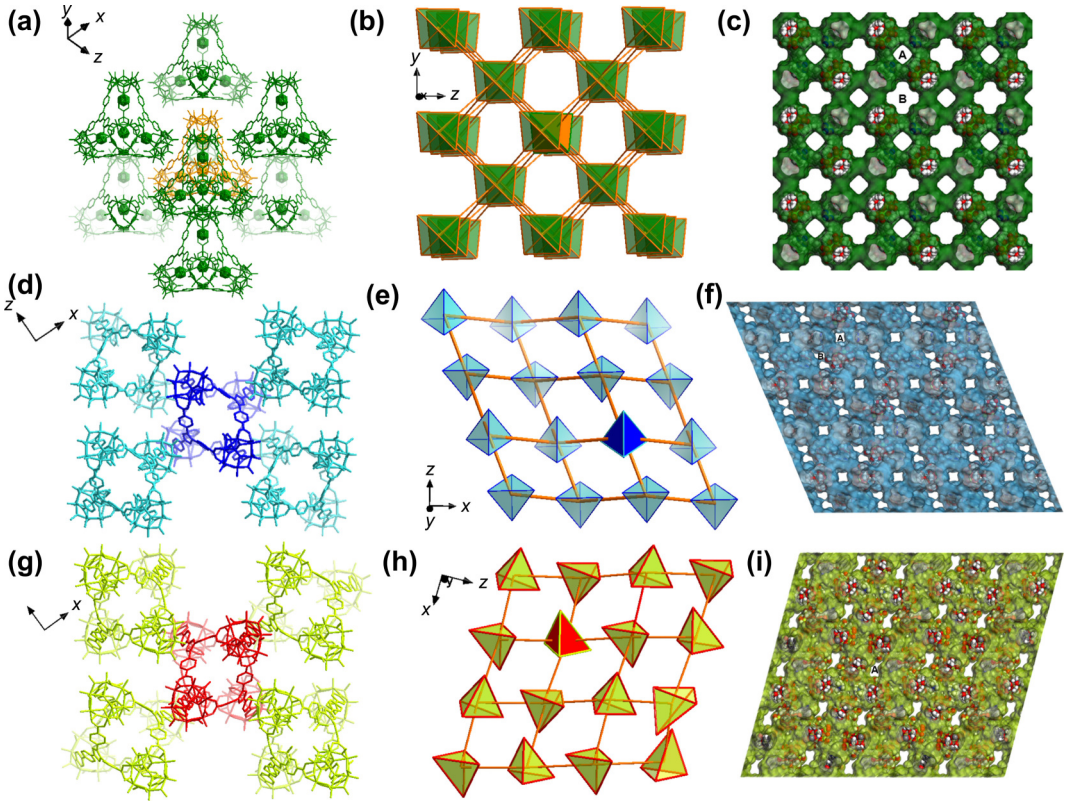

Figure 4 (a), (d), and (g) Stick presentation of a tetrahedron with its associated tetrahedra in **TMA-R-VMOT-P-1**, **TMA-I-VMOT-P-1**, and **TMA-I-VMOT-P-2**. (b) The 3D supramolecular network of **TMA-R-VMOT-P-1** exhibits a ***bcu*** topology. (e) and (h) The 2D planar-packed structures of **TMA-I-VMOT-P-1** and **TMA-I-VMOT-P-2**. (c), (f), and (i) The lattice packing arrangements of **TMA-R-VMOT-P-1**, **TMA-I-VMOT-P-1**, and **TMA-I-VMOT-P-2** display channel systems with diverse sizes.

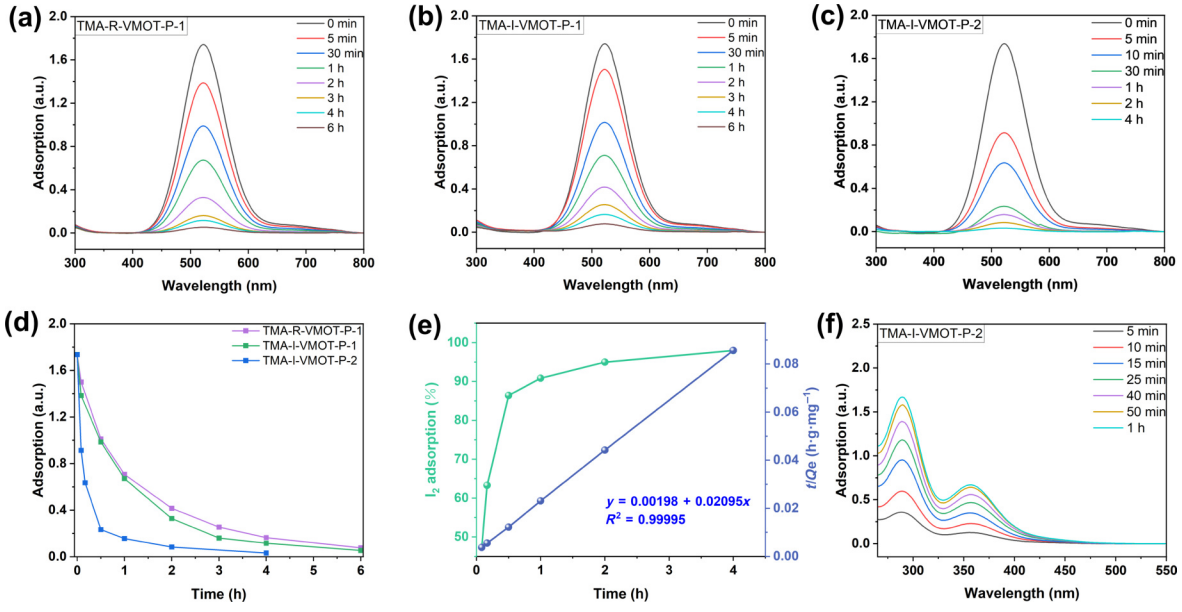

Figure 5 (a)–(c) UV–vis spectra of I_2/n-hexane solution in the presence of **TMA-R-VMOT-P-1**, **TMA-I-VMOT-P-1**, and **TMA-I-VMOT-P-2** at various time intervals. (d) Iodine adsorption performance of **TMA-R-VMOT-P-1**, **TMA-I-VMOT-P-1**, and **TMA-I-VMOT-P-2**. (e) The kinetics of the iodine adsorption in the presence of **TMA-I-VMOT-P-2**. (f) Time-dependent iodine release of **TMA-I-VMOT-P-2**.

46.70 mg·g^{-1}, respectively. For **TMA-I-VMOT-P-2**, a rapid decrease in iodine concentration was observed as a function of reaction time. Within the first 5 min, 47.31% of iodine was effectively removed, and the removal rate further increased to 97.97% after 4 h, eventually achieving adsorption equilibrium (Fig. 5(d)). A linear relationship between t/Q_t and t (R^2 = 0.99995) indicates that the kinetic data conform to the pseudo-second-order model, where t is the adsorption time and Q_t is the amount of iodine adsorbed at time t (Fig. 5(e)) [83]. Although both **TMA-I-VMOT-P-1** and **TMA-I-VMOT-P-2** contain imidazole groups and share similar

packing structures and solvent-accessible volumes, their adsorption rates exhibit remarkable differences. The observed discrepancy may be ascribed to the higher density of benzene rings and the larger cavity in **TMA-I-VMOT-P-2**, where π···I–I interactions play a vital role in enhancing I_2 adsorption. Additionally, the higher solvent-accessible volume of **TMA-I-VMOT-P-2** also contributes to improved iodine adsorption. For **TMA-R-VMOT-P-1** and **TMA-I-VMOT-P-1**, their cavity volumes are comparable. Although the nitrogen content of triazine groups is higher than that of imidazole groups, the solvent-accessible volume of **TMA-I-VMOT-P-1** exceeds that of **TMA-R-VMOT-P-1.** Thus, experimental data indicate that the iodine adsorption performance of 3D framework-packed **TMA-R-VMOT-P-1** is comparable to that of 2D planar-packed **TMA-I-VMOT-P-1**. The encapsulated iodine species in **TMA-I-VMOT-P-2** exhibited rapid release kinetics in methanol, achieving complete desorption within 2 h (Fig. 5(f)). Collectively, porous materials in this series all exhibit rapid adsorption and release of iodine species.

To examine the recyclability of **TMA-I-VMOT-P-2**, the regenerated material demonstrated stable recyclability over four consecutive cycles, maintaining a removal efficiency of > 96.3% during the regeneration process (Fig. 6(a)). Raman spectroscopic analysis was conducted on **TMA-I-VMOT-P-2** after the adsorption experiment to determine the chemical state of adsorbed iodine. As shown in Fig. 6(b), a characteristic peak at 139.6 cm^{-1} was observed, which is consistent with the stretching vibrations of I_3^- anions [84]. The structural stability of these MOPs after iodine adsorption was unambiguously verified by both Fourier transform infrared spectroscopy (FT-IR) and PXRD characterizations (Fig. 6(c) and Figs. S22 and S23 in the ESM). The SEM images at higher magnification, along with the corresponding energy dispersive X-ray spectroscopy (EDS) elemental maps, reveal a homogeneous distribution of V (turquoise), P (green), O (red), N (yellow), and the adsorbed iodine (purple) (Fig. 6(d) and Figs. S24 and S25 in the ESM).

Given the volatility of iodine (I_2), the three tetrahedral cages with embedded benzenephosphonic acid moieties were selected for iodine vapor adsorption investigations. The porous materials were separately placed in glass tubes and transferred to large sealed glass vials containing iodine, ensuring no direct contact between the solid samples and iodine. The vials were then placed in an oven at 75 °C, and the samples were weighed at fixed time intervals until constant weight was achieved, indicating adsorption equilibrium (Fig. S21 in the ESM). Overall, the adsorption trends of gaseous iodine and iodine in n-hexane solution by **TMA-R-VMOT-P-1**, **TMA-I-VMOT-P-1**, and **TMA-I-VMOT-P-2** are analogous: the isosceles tetrahedral architectures demonstrating superior adsorption efficiency over regular tetrahedral cage.

Unlike iodine adsorption in n-hexane, **TMA-I-VMOT-P-1** demonstrates better adsorption performance than **TMA-I-VMOT-P-2** for gaseous iodine. Collectively, the three materials attained adsorption equilibrium at 18 h under the specified experimental conditions (Fig. 7(a)). The equilibrium adsorption capacities of **TMA-R-VMOT-P-1**, **TMA-I-VMOT-P-1**, and **TMA-I-VMOT-P-**

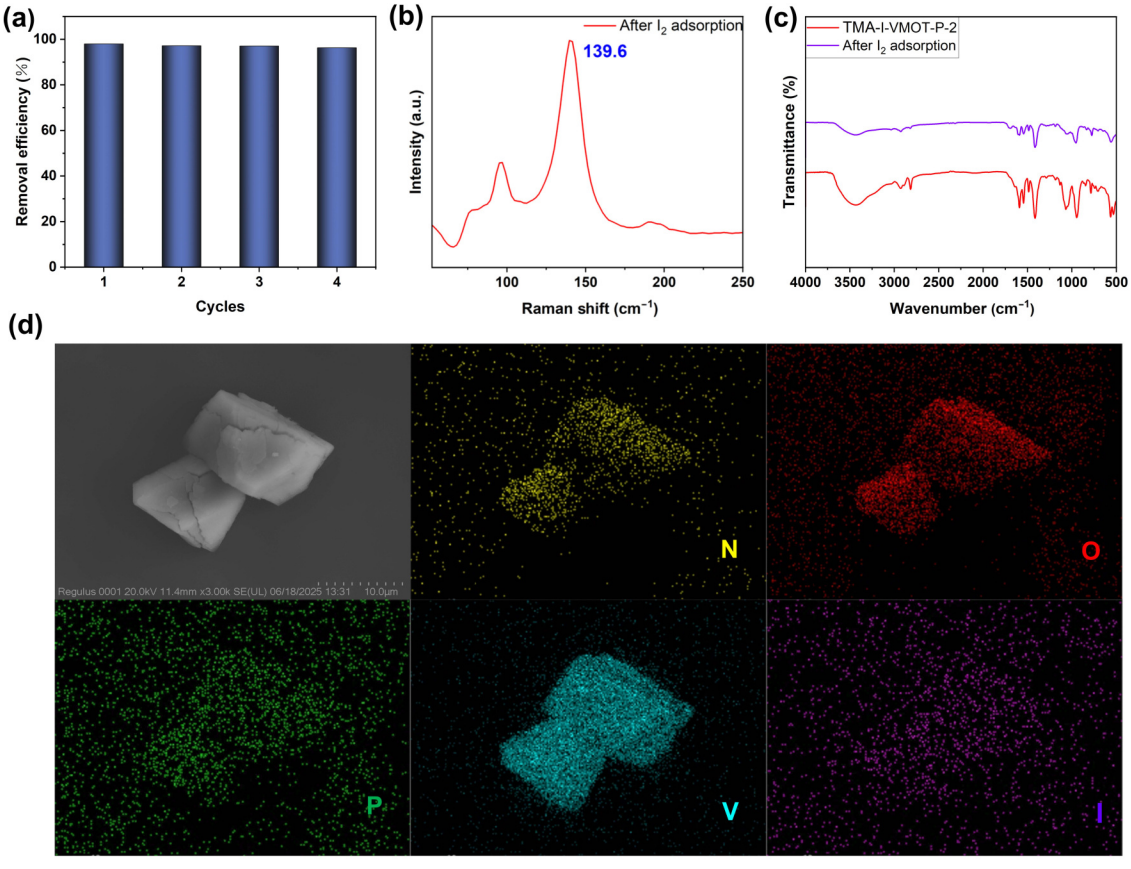

Figure 6 (a) Reusability evaluation of **TMA-I-VMOT-P-2** for iodine adsorption. (b) Raman spectrum of **TMA-I-VMOT-P-2** after iodine adsorption. (c) FT-IR spectra of **TMA-I-VMOT-P-2** before and after I_2 adsorption. (d) EDS elemental mapping images showing the distribution of N, O, P, V, and I in **TMA-I-VMOT-P-2** after I_2 adsorption.

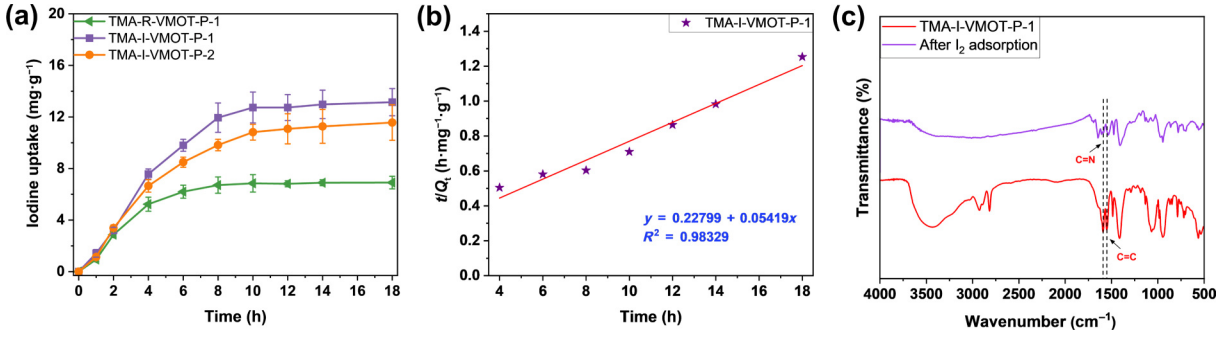

Figure 7 (a) Iodine vapor adsorption versus time for **TMA-R-VMOT-P-1**, **TMA-I-VMOT-P-1**, and **TMA-I-VMOT-P-2** at 75 °C and 1 atm. (b) Pseudo-second-order kinetic modeling results of iodine adsorption on **TMA-R-VMOT-P-1**. (c) FT-IR spectra of **TMA-I-VMOT-P-1** (red line) and iodine-adsorbed **TMA-I-VMOT-P-1** (purple line).

2 were 7.23, 14.37, and 12.80 mg·g^{-1}, respectively. The adsorption kinetic data of **TMA-I-VMOT-P-1** were analyzed using the t/Q_t equation [83], yielding a linear fit with R^2 = 0.98329, confirming that the kinetic data are consistent with the pseudo-secondary kinetic model (t: adsorption time; Q_t: the amount of iodine adsorbed at time t, Fig. 7(b)). Further FT-IR spectroscopic analysis revealed that the C=C band of **TMA-I-VMOT-P-1** shifted from 1555 to 1536 cm^{-1} after I_2 adsorption, with concomitant changes in the C=N stretching vibration, suggesting that adsorption sites are distributed on the benzene and imidazole ring of the ligand (Fig. 7(c)) [85]. The distinct adsorption behaviors of **TMA-I-VMOT-P-1** and **TMA-I-VMOT-P-2** toward gaseous iodine may be attributed to the larger cavity in **TMA-I-VMOT-P-2**, which undergoes structural collapse upon solvent removal (Fig. S26 in the ESM). Gaseous iodine adsorption experiments further confirm that functional applications can be strategically controlled by modulating structural types, highlighting the critical role of architecture–property relationships in material design.

3 Conclusions

In summary, a systematic investigation was performed to evaluate structural evolution of VMOTs driven by linker desymmetrization and SBU engineering. Replacement of the central triazine ring in symmetric tricarboxylate ligands with an imidazole ring reduces ligand symmetry and enhances conformational flexibility. Assembly of these ligands with prototype {V_6S} or expansional {V_6P} clusters yields a series of VMOTs showing structural transition from T_d to D_{2d} symmetry. Expansion of vertex clusters leads to structural fine-tuning and gives rise to diverse ligand conformations in VMOTs. Finally, iodine adsorption in n-hexane solution and as a vapor for a series of VMOTs confirms that distorted tetrahedral structures exhibit superior adsorption performance, attributable to structural feature-mediated efficacy regulation. The current work may facilitate the establishment of guidelines for the customized synthesis of MOPs with target-specific applications and improved performances.

Electronic Supplementary Material: Supplementary material (FT-IR spectra, TGA curves, and powder XRD patterns) is available in the online version of this article at https://doi.org/10.26599/NR.2025.94907902.

Data availability

All data needed to support the conclusions in the paper are presented in the manuscript and the Electronic Supplementary Material. Additional data related to this paper may be requested from the corresponding author upon request.

Acknowledgements

This research was financially supported by the Guangdong Basic and Applied Basic Research Foundation (No. 2025A1515010370) and Science and Technology Innovation Program of Hunan Province (No. 2022RC1115). Y.-H. W. thanks Wei-Jie He and the Shanghai Titan Technology Co., Ltd for providing various chemicals. Single-crystal X-ray diffraction data were acquired at the Analytical Instrumentation Center of Hunan University.

Declaration of competing interest

All the contributing authors reports no conflict of interests in this work.

Author contribution statement

M.-Y. L.: Designed and engineered the samples, conducted the experiments and data analysis, and wrote the preliminary manuscript. K.-W. T.: Crystal analysis and description. J.-P. W.: Preparation of graphical plots. H.-Z. H.: Sample characterization and analysis. J.-Y. W.: Compilation of references. C.-Q. C.: Analytical testing of samples. Y. L.: Revised the manuscript. L. C.: Revised the manuscript. Z.-Q. L.: Revised the manuscript and provided useful advice. P. Y.: Revised the manuscript and provided useful advice. Y.-H. W.: Conceived the idea of the work and revised the manuscript. All the authors have approved the final manuscript.

Use of AI statement

None.

References

[1] Sánchez-González, E.; Tsang, M. Y.; Troyano, J.; Craig, G. A.; Furukawa, S. Assembling metal-organic cages as porous materials. *Chem. Soc. Rev.* **2022**, *51*, 4876–4889.

[2] Xu, S. L.; Yan, K. C.; Xu, Z. H.; Wang, Y.; James, T. D. Fluorescent probes for targeting the Golgi apparatus: Design strategies and applications. *Chem. Soc. Rev.* **2024**, *53*, 7590–7631.

[3] Xing, C. C.; Qi, R. J.; Chang, Y.; Ma, X. M.; Lei, Y.; Zang, S. Q.; Zheng. Z. *In-situ* elemental reaction-regulated Ag_2S films enable the best thermoelectric performances. *Aggregate* **2024**, *5*, e561.

[4] Hou, X. F.; Xue, Y. L.; Yang, J. G.; Li, Z. S.; Xu, Z. H.; Li, W.; Yuan,

L. A cascade activation probe with double-enhanced near-infrared imaging for monitoring peroxynitrite fluctuations *in vivo*. *Anal. Chem.* **2024**, *96*, 17657–17664.

[5] Wang, M. Y.; Geng, H.; Zhu, J. C.; Cui, Y. B.; Zhao, S. H.; Fu, J. J.; Kou, D. X.; Sun, J.; Zhao, C. L.; Wu, S. X. et al. Hyperactive selenium source yields kesterite solar cells with 12.86% efficiency. *Adv. Funct. Mater.* **2023**, *33*, 2307389.

[6] Liu, M. Y.; Huang, Q.; Wang, S. L.; Li, Z. Y.; Li, B. Y.; Jin, S. B.; Tan, B. E. Crystalline covalent triazine frameworks by *in situ* oxidation of alcohols to aldehyde monomers. *Angew. Chem., Int. Ed.* **2018**, *57*, 11968–11972.

[7] Liu, Q.; Ren, Y. P.; Jia, H. M.; Yuan, H.; Tong, Y. P.; Kotha, S.; Mao, X. B.; Huang, Y. W.; Chen, C. Y.; Zheng, Z. et al. Vanadium carbide nanosheets with broad-spectrum antioxidant activity for pulmonary fibrosis therapy. *ACS Nano* **2023**, *17*, 22527–22538.

[8] Wu, W. N.; Chen, X.; Liu, S. S.; Bie, H. Y.; Fan, Y. C.; Wang, Y.; Xu, Z. H.; James, T. D. A dual-response fluorescent hemicyanine probe for the detection of mitochondrial hypochlorite and viscosity based on ESIPT/AIE and TICT. *Sens. Actuators B: Chem.* **2025**, *423*, 136695.

[9] Liu, L. L.; Wang, L.; Xiao, X. Y.; Yang, P.; Zhao, J. W.; Kortz, U. Structural overview and evolution paths of lacunary polyoxometalates. *Coord. Chem. Rev.* **2024**, *506*, 215687.

[10] Geng, H. Q.; Li, X. M.; Gao, X. J.; Cong, Y. L.; Liu, Q.; Li, J. J.; Guan, Y.; Wang, L. M.; He, W. W. Highly adhesive and catalytic VO_xC nanosheets with strong antibacterial activity. *Nano Today* **2023**, *52*, 101989.

[11] Gosselin, A. J.; Rowland, C. A.; Bloch, E. D. Permanently microporous metal-organic polyhedra. *Chem. Rev.* **2020**, *120*, 8987–9014.

[12] Peng, Y. G.; Chen, Y. L.; Wang, Z.; Yin, Y. Y.; Li, J. N.; Liu, H. Y.; Jiao, J. P.; Zhao, W. L.; Duan, R.; Zhang, P. et al. Selective electroreduction of carbon dioxide to ethylene over stable iodide-induced asymmetric copper sites within a metal-organic polyhedron. *Sci. Bull.*, in press, DOI: 10.1016/j.scib.2025.06.001.

[13] Lee, S.; Jeong, H.; Nam, D.; Lah, M. S.; Choe, W. The rise of metal-organic polyhedra. *Chem. Soc. Rev.* **2021**, *50*, 528–555.

[14] Pan, M.; Wu, K.; Zhang, J. H.; Su, C. Y. Chiral metal-organic cages/containers (MOCs): From structural and stereochemical design to applications. *Coord. Chem. Rev.* **2019**, *378*, 333–349.

[15] Li, X. X.; Zhao, D.; Zheng, S. T. Recent advances in POM-organic frameworks and POM-organic polyhedra. *Coord. Chem. Rev.* **2019**, *397*, 220–240.

[16] Liu, J. J.; Wang, Z. F.; Cheng, P.; Zaworotko, M. J.; Chen, Y.; Zhang, Z. J. Post-synthetic modifications of metal-organic cages. *Nat. Rev. Chem.* **2022**, *6*, 339–356.

[17] Chang, Q.; Meng, X. Y.; Ruan, W. J.; Feng, Y. Q.; Li, R.; Zhu, J. Y.; Ding, Y.; Lv, H. J.; Wang, W.; Chen, G. Y. et al. Metal-organic cages with $\{SiW_9Ni_4\}$ polyoxotungstate nodes. *Angew. Chem., Int. Ed.* **2022**, *61*, e202117637.

[18] Li, J.; Feng, Y. Q.; Fu, F. Y.; Xin, X.; Yang, G. Y.; Lv, H. J. Polyoxometalate-organic cage with $\{Ni_4SiW_9\}$ node for photocatalytic hydrogen evolution. *Chin. Chem. Lett.* **2024**, *35*, 108736.

[19] Kalmutzki, M. J.; Hanikel, N.; Yaghi. O. M. Secondary building units as the turning point in the development of the reticular chemistry of MOFs. *Sci. Adv.* **2018**, *4*, eaat9180.

[20] Kondinski, A.; Menon, A.; Nurkowski, D.; Farazi, F.; Mosbach, S.; Akroyd, J.; Kraft, M. Automated rational design of metal-organic polyhedra. *J. Am. Chem. Soc.* **2022**, *144*, 11713–11728.

[21] El-Sayed, E. S. M.; Yuan, Y. D.; Zhao, D.; Yuan, D. Q. Zirconium metal-organic cages: Synthesis and applications. *Acc. Chem. Res.* **2022**, *55*, 1546–1560.

[22] Huang, Y. H.; Lu, Y. L.; Ruan, J.; Zheng, S. P.; Zhang, X. D.; Liu, C. H.; Qin, Y. H.; Cao, Z. M.; Jiao, Z. W.; Xu, H. S. et al. Dynamic metallosupramolecular cages containing 12 adaptable pockets for high-order guest binding beyond biomimicry. *J. Am. Chem. Soc.* **2023**, *145*, 23361–23371.

[23] Abednatanzi, S.; Derakhshandeh, P. G.; Depauw, H.; Coudert, F. X.; Vrielinck, H.; Van Der Voort, P.; Leus, K. Mixed-metal metal-organic frameworks. *Chem. Soc. Rev.* **2019**, *48*, 2535–2565.

[24] He, W. W.; Li, S. L.; Zang, H. Y.; Yang, G. S.; Zhang, S. R.; Su, Z. M.; Lan, Y. Q. Entangled structures in polyoxometalate-based coordination polymers. *Coord. Chem. Rev.* **2014**, *279*, 141–160.

[25] Jiang, L.; Lin, L.; Wang, Z. H.; Ai, H. Y.; Jia, J. T.; Zhu, G. S. Constructing isoreticular metal-organic frameworks by silver-carbon bonds. *J. Am. Chem. Soc.* **2024**, *146*, 22930–22936.

[26] Zhao, J.; Gong, J. W.; Wei, J. N.; Yang, Q.; Li, G. J.; Tong, Y. P.; He, W. W. Metal organic framework loaded fluorescent nitrogen-doped carbon nanozyme with light regulating redox ability for detection of ferric ion and glutathione. *J. Colloid Interface Sci.* **2022**, *618*, 11–21.

[27] Li, M. Y.; Liu, X.; Che, Y.; Xing, H. Z.; Sun, F. F.; Zhou, W.; Zhu, G. S. Controlled partial linker thermolysis in metal-organic framework UiO-66-NH_2 to give a single-site copper photocatalyst for the functionalization of terminal alkynes. *Angew. Chem., Int. Ed.* **2023**, *62*, e202308651.

[28] Schoedel, A.; Li, M.; Li, D.; O'Keeffe, M.; Yaghi, O. M. Structures of metal-organic frameworks with rod secondary building units. *Chem. Rev.* **2016**, *116*, 12466–12535.

[29] Zhang, C. H.; Formalik, F.; Lv, D. F.; Sha, F. R.; Kirlikovali, K. O.; Wang, X. L.; Tang, X. H.; Su, S. Y.; Xie, H. M.; Chen, Y. W. et al. Lowering linker symmetry to access zirconium metal-organic frameworks for inverse alkane/alkene separations. *Angew. Chem.* **2025**, *137*, e202424260.

[30] Xia, H. L.; Zhou, K.; Yu, L.; Wang, H.; Liu, X. Y.; Proserpio, D. M.; Li, J. Customized synthesis: Solvent-and acid-assisted topology evolution in zirconium-tetracarboxylate frameworks. *Inorg. Chem.* **2022**, *61*, 7980–7988.

[31] Wang, Z. W.; Zhao, Q.; Chen, C. A.; Sun, J. J.; Lv, H. J.; Yang, G. Y. Chiral $\{Ni_6PW_9\}$ cluster-organic framework: Synthesis, structure, and properties. *Inorg. Chem.* **2022**, *61*, 7477–7483.

[32] Wang, X. Y.; Chen, W. C.; Shao, K. Z.; Wang, X. L.; Zhao, L.; Su, Z. M. An octahedral polyoxomolybdate-organic molecular cage. *Chem. Commun.* **2021**, *57*, 1042–1045.

[33] Liu, G. L.; Ju, Z. F.; Yuan, D. Q.; Hong, M. C. *In situ* construction of a coordination zirconocene tetrahedron. *Inorg. Chem.* **2013**, *52*, 13815–13817.

[34] Liu, M.; Liao, W. P.; Hu, C. H.; Du, S. C.; Zhang, H. J. Calixarene-based nanoscale coordination cages. *Angew. Chem.* **2012**, *124*, 1617–1620.

[35] Zhang, Y. T.; Gan, H. M.; Qin, C.; Wang, X. L.; Su, Z. M.; Zaworotko, M. J. Self-assembly of Goldberg polyhedra from a concave $[WV_5O_{11}(RCO_2)_5(SO_4)]^{3-}$ building block with 5-fold symmetry. *J. Am. Chem. Soc.* **2018**, *140*, 17365–17368.

[36] Cavka, J. H.; Jakobsen, S.; Olsbye, U.; Guillou, N.; Lamberti, C.; Bordiga, S.; Lillerud, K. P. A new zirconium inorganic building brick forming metal organic frameworks with exceptional stability. *J. Am. Chem. Soc.* **2008**, *130*, 13850–13851.

[37] Wang, Y. H.; Tong, K. W.; Chen, C. Q.; Du, J.; Yang, P. Weak interaction-steered evolution of polyoxovanadate-based metal-organic polyhedra from transformation via interlock to packing. *Chin. Chem. Lett.* **2024**, *35*, 109066.

[38] Zhou, Y. J.; Yang, J.; Jie, K. C. Macrocyclic arene-based metal-organic cages. *Coord. Chem. Rev.* **2025**, *539*, 216726.

[39] Perona-Bermejo, C.; Vismara, R.; Padial, N. M.; Almora-Barrios, N.; Maldonado, C. R.; Bandosz, T. J.; Garrido-Barros, P.; Carmona, F. J.; Navarro, J. A. R. Metalorganic polyhedra polyoxometalate hybrid salts for tandem photooxidative-hydrolytic pesticide detoxification. *Adv. Funct. Mater.* **2024**, *34*, 2405785.

[40] Wang, Y. H.; Tong, K. W.; Xiong, S. R.; Chen, C. Q.; Song, Y. H.; Yang, P. Steerable structural evolvement and adsorption behavior of metastable polyoxovanadate-based metal-organic polyhedra. *Inorg. Chem.* **2024**, *63*, 20984–20992.

[41] Tong, K. W.; Wang, Y. H.; Du, J.; Chen, C. Q.; Lan, Y. Q.; Yang, P.

Splicing them together: Construction of polyoxovanadate-organic polyhedra-based pyrgoscages and catenane. *Angew. Chem., Int. Ed.* **2025**, *64*, e202504424.

[42] Su, K. Z.; Wu, M. Y.; Yuan, D. Q.; Hong, M. C. Interconvertible vanadium-seamed hexameric pyrogallol[4]arene nanocapsules. *Nat. Commun.* **2018**, *9*, 4941.

[43] Xiao, Z. F.; Drake, H. F.; Rezenom, Y. H.; Cai, P. Y.; Zhou, H. C. Structural manipulation of a zirconocene-based porous coordination cage using external and host-guest stimuli. *Small Struct.* **2022**, *3*, 2100133.

[44] Zhong, Y. H.; Ye, Z. M.; Sha, F. R.; Xie, H. M.; Wang, X. L.; Zhang, C. H.; Lv, D. F.; Chen, Y. W.; Li, Z. B.; Farha, O. K. Reduced-symmetry ligand constructed Y-based metal-organic framework for inverse propane/propylene separation. *ACS Materials Lett.* **2024**, *6*, 5348–5353.

[45] Schneemann, A.; Bon, V.; Schwedler, I.; Senkovska, I.; Kaskel, S.; Fischer, R. A. Flexible metal-organic frameworks. *Chem. Soc. Rev.* **2014**, *43*, 6062–6096.

[46] Ni, L. B.; Gu, J.; Jiang, X. Y.; Xu, H. J.; Wu, Z.; Wu, Y. C.; Liu, Y.; Xie, J.; Wei, Y. G.; Diao, G. W. Polyoxometalate-cyclodextrin-based cluster-organic supramolecular framework for polysulfide conversion and guest-host recognition in lithium-sulfur batteries. *Angew. Chem., Int. Ed.* **2023**, *62*, e202306528.

[47] Xiao, F. P.; Meng, X. G.; Wang, L. S.; Hao, J.; Lv, C. L.; Wei, Y. G. Polyoxometalatocrown ether: A new type of metallacrown ether based on polyoxometalate. *Polyoxometalates* **2024**, *3*, 9140055.

[48] Sheng, H. X.; Lin, B. Y.; Chen, C. Q.; Du, J.; Yang, P. From confined growth to enhanced peroxidase-like activity: Nucleation of a phosphate-mediated Fe^{III}–Ce^{III}-oxo cluster inside the $\{P_8W_{48}\}$ nanoreactor. *Polyoxometalates* **2024**, *3*, 9140060.

[49] Yan, J. L.; Zhang, L.; Wu, W. N.; Wang, Y.; Xu, Z. H. A novel AIRE-based fluorescent ratiometric probe with endoplasmic reticulum-targeting ability for detection of hypochlorite and bioimaging. *Bioorg. Chem.* **2023**, *131*, 106319.

[50] Du, Y. P.; Jia, M. G.; Zhang, X.; Ma, M. Z.; Zhang, X. F.; Li, C. X.; Wang, S. K.; Zhang, J. W.; Li, D. P.; He, W. W. et al. Graphene oxide covered WO_3 nanosheet arrays as photoelectrode for photoelectrochemical detection of trace H_2O_2. *ACS Appl. Nano Mater.* **2024**, *7*, 7896–7905.

[51] Song, Y. F.; Yan, K. C.; Liu, P.; Wu, W. N.; Zhao, X. L.; Thet, N.; Wang, Y.; Fan, Y. C.; Xu, Z. H.; James, T. D. et al. Ferrocene-chalcone-based probe for the fluorescence and electrochemical dual-mode detection of carboxylesterase. *Sens. Actuators B: Chem.* **2024**, *405*, 135284.

[52] Liang, Y.; Fang, Y.; Cui, Y.; Zhou, H. C. A stable biocompatible porous coordination cage promotes *in vivo* liver tumor inhibition. *Nano Res.* **2021**, *14*, 3407–3415.

[53] Gu, Y. Q.; Li, Q.; Zang, D. J.; Huang, Y. C.; Yu, H.; Wei, Y. G. Light-induced efficient hydroxylation of benzene to phenol by quinolinium and polyoxovanadate-based supramolecular catalysts. *Angew. Chem., Int. Ed.* **2021**, *60*, 13310–13316.

[54] Ding, J. H.; Liu, Y. F.; Tian, Z. T.; Lin, P. J.; Yang, F.; Li, K.; Yang, G. P.; Wei, Y. G. Uranyl-silicotungstate-containing hybrid building units $\{\alpha\text{-}SiW_9\}$ and $\{\gamma\text{-}SiW_{10}\}$ with excellent catalytic activities in the three-component synthesis of dihydropyrimidin-2(1*H*)-ones. *Inorg. Chem. Front.* **2023**, *10*, 3195–3201.

[55] Gao, J. P.; Qi, Z. K.; Zhang, F. Q.; Zhang, X. M. $[MoO_4]^{2-}$-templated D_{4h}-symmetric sandwich Ag_{13} nanocluster coprotected with thiolate and phosphine. *Polyoxometalates* **2023**, *2*, 9140028.

[56] Zhang, Y. T.; Wang, X. L.; Li, S. B.; Gong, Y. R.; Song, B. Q.; Shao, K. Z.; Su, Z. M. Anderson-like alkoxo-polyoxovanadate clusters serving as unprecedented second building units to construct metal-organic polyhedra. *Chem. Commun.* **2016**, *52*, 9632–9635.

[57] Zhang, Y. T.; Li, S. B.; Wang, X. L.; Gong, Y. R.; Shao, K. Z.; Su, Z. M. Synthesis, structures, and magnetic properties of metal-organic polyhedra based on unprecedented $\{V_7\}$ isopolyoxometalate clusters. *Dalton Trans.* **2016**, *45*, 14898–14901.

[58] Guo, J.; Chang, Q.; Liu, Z. W.; Wang, Y. M.; Liu, C. H.; Wang, M.; Huang, D. M.; Chen, G. Y.; Zhao, H. M.; Wang, W. et al. How to not build a cage: Endohedral functionalization of polyoxometalate-based metal-organic polyhedral. *Chem. Sci.* **2021**, *12*, 7361–7368.

[59] Guo, J.; Liu, J. R.; Cui, Y. C.; Liu, C. H.; Wang, Y. M.; Wang, M.; Huang, D. M.; Chen. G. Y.; Wan, W.; Xia, D. B. et al. Timing matters: Pre-assembly versus post-assembly functionalization of a polyoxovanadate-organic cuboid. *Chem. Sci.* **2022**, *13*, 5718–5725.

[60] Zhang, Z. J.; Wojtas, L.; Zaworotko, M. J. Organic-inorganic hybrid polyhedra that can serve as supermolecular building blocks. *Chem. Sci.* **2014**, *5*, 927–931.

[61] Zhang, Z. X.; Gao, W. Y.; Wojtas, L.; Zhang, Z. J.; Zaworotko, M. J. A new family of anionic organic–inorganic hybrid doughnut-like nanostructures. *Chem. Commun.* **2015**, *51*, 9223–9226.

[62] Gan, H. M.; Bao, L. Y.; Xu, N.; Hou, B. S.; Wang, X. L.; Su, Z. M. Self-assembly engineering of fullerene-like polyhedra: V_{60}, V_{66}, V_{72} from $\{MV_5\}$ pentagonal second building block. *Adv. Sci.* **2025**, *12*, 2408863.

[63] Wang, Y. H.; Tong, K. W.; Chen, C. Q.; Du, J.; Yang, G. P.; Yang, P. Controlling the structural and adsorption features of polyoxovanadate-based metal-organic clusters by adjustable template effect. *Inorg. Chem. Front.* **2024**, *11*, 2726–2734.

[64] Gan, H. M.; Xu, N.; Qin, C.; Sun, C. Y.; Wang, X. L.; Su, Z. M. Equi-size nesting of platonic and archimedean metal-organic polyhedra into a twin capsid. *Nat. Commun.* **2020**, *11*, 4103.

[65] Gong, Y. R.; Zhang, Y. T.; Qin, C.; Sun, C. Y.; Wang, X. L.; Su, Z. M. Bottom-up construction and reversible structural transformation of supramolecular isomers based on large truncated tetrahedra. *Angew. Chem.* **2019**, *131*, 790–794.

[66] Xu, N.; Gan, H. M.; Qin, C.; Wang, X. L.; Su, Z. M. From octahedral to icosahedral metal-organic polyhedra assembled from two types of polyoxovanadate clusters. *Angew. Chem., Int. Ed.* **2019**, *58*, 4649–4653.

[67] Gong, Y. R.; Qin, C.; Zhang, Y. T.; Sun, C. Y.; Pan, Q. H.; Wang, X. L.; Su, Z. M. Face-directed assembly of molecular cubes: *In situ* substitution of a predetermined concave cluster. *Angew. Chem.* **2020**, *132*, 22218–22222.

[68] Yang, Y.; Fu, Y. M.; Wu, S. X.; Zhao, L.; Qin, C.; Wang, X. L.; Su, Z. M. Endohedral functionalization for structural transformation of polyoxovanadate-based metal-organic cube. *Inorg. Chem.* **2023**, *62*, 648–652.

[69] Yang, Y.; Fu, Y. M.; Tian, Y. R.; Zhao, L.; Qin, C.; Wang, X. L.; Su, Z. M. Efficient iodine capture by metal-organic cubes based on hexanuclear vanadium clusters. *Inorg. Chem. Front.* **2023**, *10*, 6221–6228.

[70] Gong, Y. R.; Chen, W. C.; Zhao, L.; Shao, K. Z.; Wang, X. L.; Su, Z. M. Functionalized polyoxometalate-based metal-organic cuboctahedra for selective adsorption toward cationic dyes in aqueous solution. *Dalton Trans.* **2018**, *47*, 12979–12983.

[71] Guo, B. B.; Li, F. G.; Wang, C. M.; Zhang, L. L.; Sun, D. F. A rare (3, 12)-connected zirconium metal-organic framework with efficient iodine adsorption capacity and pH sensing. *J. Mater. Chem. A* **2019**, *7*, 13173–13179.

[72] Xin, X. L.; Ai, J.; Li, F. G.; Zhao, J. Q.; Zhang, L. L. An imidazole functionalized copper(II)-organic framework for highly selective sensing of picric acid and metal ions in water. *Appl. Organomet. Chem.* **2020**, *34*, e5803.

[73] Li, F. G.; Liu, C. P.; Yuan, D. Q.; Dai, F. N.; Wang, R. M.; Wang, Z. K.; Lu, X. Q.; Sun, D. F. Ultrahigh hydrogen uptake in an

interpenetrated Zn_4O-based metal-organic framework. *CCS Chem.* **2022**, *4*, 832–837.

[74] Hang, X. X.; Liu, B.; Zhu, X. F.; Wang, S. T.; Han, H. T.; Liao, W. P.; Liu, Y. L.; Hu, C. H. Discrete $\{Ni_{40}\}$ coordination cage: A calixarene-based Johnson-type (J_{17}) hexadecahedron. *J. Am. Chem. Soc.* **2016**, *138*, 2969–2972.

[75] Zhang, X. R.; Maddock, J.; Nenoff, T. M.; Denecke, M. A.; Yang, S. H.; Schröder, M. Adsorption of iodine in metal-organic framework materials. *Chem. Soc. Rev.* **2022**, *51*, 3243–3262.

[76] Jia. M. W.; Li, J. T.; Che, S. T.; Kan, L.; Li, G. H.; Liu, Y. L. Two Cu_xI_y-based copper-organic frameworks with multiple secondary building units (SBUs): Structure, gas adsorption and impressive ability of I_2 sorption and release. *Inorg. Chem. Front.* **2019**, *6*, 1261–1266.

[77] Sava, D. F.; Chapman, K. W.; Rodriguez, M. A.; Greathouse, J. A.; Crozier, P. S.; Zhao, H. Y.; Chupas, P. J.; Nenoff, T. M. Competitive I_2 sorption by Cu-BTC from humid gas streams. *Chem. Mater.* **2013**, *25*, 2591–2596.

[78] Chu, Q. Q.; Lin, Y.; Wang, L. Y.; Gong, Y. R.; Wang, X. L.; Pan, Q. H.; Yang, W. T.; Su, Z. M. Investigation of iodine adsorption based on isomeric polyoxovanadate-based metal-organic cages. *Polyhedron* **2024**, *257*, 117008.

[79] Cheng, K.; Li, H. L.; Wang, J. R.; Li, P. Z.; Zhao, Y. L. From supramolecular organic cages to porous covalent organic frameworks for enhancing iodine adsorption capability by fully exposed nitrogen-rich sites. *Small* **2023**, *19*, 2301998.

[80] Hou, Y. H.; Chen, H. P.; Zhang, T.; Gong, Y. R.; Zheng, H. Y.; Hou, B. S.; Wang, X. L. Construction and in-cage modification of metal-organic polyhedra based on Anderson-like polyoxovanadate clusters. *J. Coord. Chem.* **2022**, *75*, 1781–1790.

[81] Maglic, J. B.; Lavendomme, R. MoloVol: An easy-to-use program for analyzing cavities, volumes and surface areas of chemical structures. *J. Appl. Crystallogr.* **2022**, *55*, 1033–1044.

[82] Spek, A. L. *PLATON* SQUEEZE: A tool for the calculation of the disordered solvent contribution to the calculated structure factors. *Acta Crystallogr. C Struct. Chem.* **2015**, *71*, 9–18.

[83] Qin, J. X.; Zhang, W.; Chen, Y. T.; Liu, R.; Fan, Y. R. Zinc-based triazole metal complexes for efficient iodine adsorption in water. *Environ. Sci. Pollut. Res.* **2021**, *28*, 28797–28807.

[84] Xie, Y. Q.; Pan, T. T.; Lei, Q.; Chen, C. L.; Dong, X. L.; Yuan, Y. Y.; Shen, J.; Cai, Y. C.; Zhou, C. H.; Pinnau, I. et al. Ionic functionalization of multivariate covalent organic frameworks to achieve an exceptionally high iodine-capture capacity. *Angew. Chem., Int. Ed.* **2021**, *60*, 22432–22440.

[85] Luo, D.; He, Y. L.; Tian, J. Y.; Sessler, J. L.; Chi, X. D. Reversible iodine capture by nonporous adaptive crystals of a bipyridine cage. *J. Am. Chem. Soc.* **2022**, *144*, 113–117.